

Three-dimensional Vorticity Effects on Extinction Behavior of Laminar Flamelets

Wes Hellwig, Xian Shi, William A. Sirignano

*Department of Mechanical and Aerospace Engineering
University of California, Irvine, 92697*

July 5, 2023

Abstract

A recently proposed rotational flamelet model (Sirignano [1, 2, 3]) is developed and tested in an improved framework of detailed chemistry and transport models. The rotational flamelet model, in contrast to standard two-dimensional or axisymmetric irrotational models, incorporates the effects of shear strain and vorticity on local flame behavior and is three-dimensional by nature. A similarity solution (Sirignano [1, 2, 3]) is used to reduce the three-dimensional governing equations to a set of ODEs involving a transformation to a non-Newtonian reference frame. Multiple flamelet cases including both diffusion and premixed flames are tested to demonstrate the impact of vorticity on flame structure, extinction, and local mixture composition. For diluted hydrogen flames where the location of minimum density coincides with the location of peak temperature, the centrifugal force induced by vorticity reduces mass flow rate in the flame zone, effectively lowering the local strain rate. This results in increased residence time, thus extending flammability limits and reducing burning rates. For pure hydrogen-oxygen flames where minimum density lies between the flame zone and the fuel inlet boundary, centrifugal forces do not significantly modify flame behavior. Stable and unstable branches of extinction curves (S-curves) are computed which showcase how vorticity extends flammability limits. These capabilities of the rotational flamelet model reveal that vital physics are currently missing from two-dimensional, irrotational, constant-density flamelet models. The improvements noted regarding detailed chemical kinetics, transport formulation, and thermo-physical properties bring the new flamelet model to par in these areas with existing models, while surpassing existing models in terms of physical emulation.

Keywords— Flamelet Modeling, Vorticity, Three-dimensionality

Corresponding Author:

whellwig@uci.edu (Wes Hellwig)

1 Introduction

Combustion processes in gas turbine and rocket engines involve high mass fluxes and are inherently turbulent, making simulations of such processes challenging. For flows of these scales, the computation time of direct numerical simulations (DNS) is prohibitively costly, precipitating the need for large-eddy simulations (LES) or Reynolds-averaged Navier-Stokes (RANS) simulations. These techniques, as opposed to DNS, do not resolve all length scales of the turbulent flow, instead filtering smaller length scales (sub-scale) below the mesh size (LES) or neglecting fluctuating components of flow variables (RANS), and modeling the unresolved processes. The approach of flamelet models is one of the most widely used techniques to model the sub-scale chemical processes. The classical flamelet theory considers turbulent flames existing in the diffusion layer between oxidizer and fuel interfaces as an ensemble of thin, highly sheared, reactive zones, where each may be approximated by a counterflow diffusion flame (flamelet). The ensemble of flamelets implies that any one flamelet exists only in a small section of a turbulent interface, thus avoiding the flawed assumption of chemical equilibrium throughout the flow. The flamelet approximation is governed by the assumption that flamelet chemical and diffusion time scales are significantly shorter than resolved-flow time scales. Thereby, a quasi-steady assumption for chemical processes can be made for each flamelet.

The use of flamelets in LES and RANS provides a significant improvement in computational efficiency; however, the many assumptions on which existing flamelet theories are built cause limitations. Existing models (e.g., [4]) assume an axisymmetric or planar geometry and corresponding strain field while frequent three-dimensionality has been observed [5, 6, 7, 8, 9]. As the length scales decrease in turbulent flows, the magnitudes of shear strain and vorticity increase, suggesting that centrifugal forces could affect flamelets appreciably. These rotational effects are neglected in existing models. Furthermore, consideration of variable density compounds centrifugal effects, another effect that is neglected in current models [10, 11]. Additionally, classical flamelet theories assume, a priori, a diffusion or premixed flamelet while LES results indicate premixed, partially premixed, diffusion, and multi-branched flames can all appear at any time or location in a turbulent reacting flow [12, 13, 14, 15, 16, 17]. In the flamelet progress variable model (FPV), [4] included the upper and middle branches of the temperature versus scalar dissipation rate curve, which addressed the issue of unsteady flamelet behavior such as extinction and re-ignition. Pierce and Moin also introduced the progress variable (which tracks the global progression of the locally reacting mixture as a function of scalar dissipation rate at maximum flamelet temperature), greatly simplifying computations by governing this variable with a partial differential equation on the resolved scale. While a significant improvement to flamelet modeling, the FPV has drawn certain criticisms with its definition of progress variable (based on an arbitrary choice of physical parameters), constant-density approximation, and consideration only of normal strain imposed on the flame region while neglecting shear strain, thereby assuming irrotationality of the in-flowing streams.

Sirignano [1, 2, 3] addressed these issues with a new flamelet model, outlining five foundational criteria that the improved model must abide by. These are: 1) non-premixed, premixed, and multi-branched flames should be determined rather than prescribed; 2) the effects of shear strain and vorticity should be considered; 3) the shear strain and vorticity applied in the sub-grid model should be determined from the resolved scale without a contrived progress variable; 4) the model should be three-dimensional and not limited to axisymmetric or planar cases; and 5) variable density should be considered [1]. Sirignano demonstrated this new model using one-step chemical kinetics for propane-oxygen combustion, Fickian diffusion, and a similarity solution in the non-Newtonian

reference frame that reduces the three-dimensional governing equations to a set of ODEs. The inclusion of centrifugal force caused by vorticity in the momentum equations was shown to reduce mass flux into the counterflow by creating a more adverse pressure gradient. Reduction of the in-flowing mass fluxes increases the residence time which reduces the burning rate but extends flammability limits. Additionally, the centrifugal force alters the out-flowing directions of gas based on density. The lighter gas (the product of combustion) tends to flow out along the vorticity axis because its low inertia is overpowered by the centrifugal force. Conversely, higher-density gas (unburned propellants and some low-temperature combustion products) flows outward in the plane affected by vorticity.

The goals of the current study are to improve the three-dimensional rotational flamelet model by: 1) using multi-step chemical kinetic models to calculate chemical source terms; 2) replacing the binary Fickian diffusion formulation with the multi-component diffusion formulation that considers the gradients of all species when calculating diffusion flux; 3) treating the governing equations in their full form, i.e. making no assumptions of constant or proportional thermo-physical properties; 4) developing both the stable and unstable branch of the flammability curves; 5) provide a more detailed description of the dependence of flammability limits on normal strain rates and vorticity; and 6) compare nozzle counterflow geometry to freestream counterflow geometry.

The analytical and computational analysis is presented in Section 2 and the comparison with nozzle-based counterflows is presented in Section 3. The results for diffusion flames and premixed flames are given in Sections 4 and 5, separately, and concluding remarks are presented in Section 6.

2 Methods

The governing equations for unsteady 3D flow, shown below, retain the non-Newtonian reference frame used by Sirignano; the vorticity vector aligns with the z -axis while the ξ and χ axes rotate about z at a constant angular speed, $d\theta/dt = \omega_k/2$ where ω_k is the Kolmogorov vorticity. See Figure 1.

$$\frac{\partial \rho}{\partial t} + \frac{\partial(\rho u_j)}{\partial x_j} = 0 \quad (1)$$

$$\rho \frac{\partial u_i}{\partial t} + \rho u_j \frac{\partial u_i}{\partial x_j} + \frac{\partial p}{\partial x_i} = \frac{\partial \tau_{ij}}{\partial x_j} + \rho a_i \quad (2)$$

$$\frac{\partial(\rho h)}{\partial t} + \frac{\partial}{\partial x_j} (\rho u_j h) + \frac{\partial}{\partial x_j} \sum_{m=1}^N \rho v_{m,j} Y_m h_m - \frac{\partial p}{\partial t} - u_j \frac{\partial p}{\partial x_j} = \frac{\partial}{\partial x_j} \left(\lambda \frac{\partial T}{\partial x_j} \right) - \rho \sum_{m=1}^N h_{f,m} \dot{\omega}_m \quad (3)$$

$$\frac{\partial(\rho Y_m)}{\partial t} + \frac{\partial}{\partial x_j} (\rho Y_m u_j) + \frac{\partial}{\partial x_j} (\rho Y_m v_{m,j}) = \rho \dot{\omega}_m ; \quad m = 1, 2, 3, \dots, N \quad (4)$$

In-flows to the counterflow enter along the χ axis. Velocity components and spatial variables in this rotating frame are $u_i = u_\xi, u_\chi, w$ and $x_i = \xi, \chi, z$ respectively. The centrifugal acceleration is $a_i = \langle \xi \omega_k^2/4, \chi \omega_k^2/4, 0 \rangle$. The quantities $\rho, p, T, h, h_m, v_m, Y_m, \lambda, c_p, c_{p_m}, h_{f,m}$, and $\dot{\omega}_m$ are density, pressure, temperature, mixture specific enthalpy, specific enthalpy of species m , diffusion

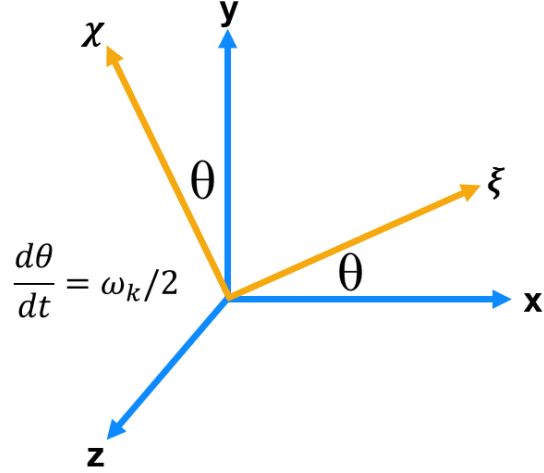


Figure 1: Coordinate transformation.

velocity of species m , mass fraction of species m , mixture thermal conductivity, mixture specific heat, specific heat of species m , heat of formation of species m , and chemical reaction rate of species m , respectively. The analysis will use the low-Mach number approximations, i.e., terms on the order of kinetic energy per unit mass are small compared to thermal energy and therefore are negligible. Additionally, viscous dissipation terms are assumed to be negligible except for cases with large strain rates which are not the subject of this paper.

u_j, v_m	t	x_i	ρ	$h, h_m, h_{f,m}$	p	$\dot{\omega}_m$	μ	λ	c_p, c_{p_m}	ω_k
$\sqrt{\frac{S^* \mu_\infty}{\rho_\infty}}$	S^{*-1}	$\sqrt{\frac{\mu_\infty}{\rho_\infty S^*}}$	ρ_∞	$c_{p_\infty} T_\infty$	$S^* \mu_\infty$	S^*	μ_∞	$\mu_\infty c_{p_\infty}$	c_{p_∞}	S^*

Table 1: Normalization factors.

The non-dimensional forms of the governing equations remain identical to Equations 1-4 when proper normalization factors are chosen. See Table 1 for details. Note, dimensional strain rates imposed on the ξ and z axes are respectively S_1^* and S_2^* and are each normalized by the principal strain rate at ∞ along the χ axis $S^* \equiv S_1^* + S_2^*$ forming non-dimensional strain rates S_1 and S_2 . Total specific enthalpy is defined as $h_m^0 \equiv h_m + h_{f,m}$ and is normalized according to Table 1. The similarity solution derived by Sirignano is used to reduce the 3D governing equations to a set of ODEs employing the density-weighted Illingworth transformation $\eta \equiv \int_0^\chi \rho(\chi') d\chi'$. In the similar form, $u_\xi = S_1 \xi (df_1/d\eta)$, $w = S_2 z (df_2/d\eta)$, and $u_\chi = -f/\rho$ with $f \equiv S_1 f_1 + S_2 f_2$. The final forms of the governing equations with boundary conditions are presented below. Note, the centrifugal effect is incorporated in the last term of Equation 5 and in the corresponding boundary condition at $\eta = -\infty$ in Equation 11.

$$\rho \mu f_1''' + f_1''(\rho \mu)' + f f_1'' + S_1 \left(\frac{1}{\rho} - (f_1')^2 \right) + \frac{\omega_k^2}{4S_1} \left(1 - \frac{1}{\rho} \right) = 0 \quad (5)$$

$$\rho\mu f_2''' + f_2''(\rho\mu)' + f f_2'' + S_2 \left(\frac{1}{\rho} - (f_2')^2 \right) = 0 \quad (6)$$

$$fT' + \frac{1}{c_p}(\rho\lambda T')' - \frac{1}{c_p}T' \sum_{m=1}^N J_m c_{p_m} - \frac{1}{c_p} \sum_{m=1}^N h_m^0 \dot{\omega}_m = 0 ; \quad m = 1, 2, 3, \dots, N \quad (7)$$

$$fY_m' - J_m' + \dot{\omega}_m = 0 ; \quad m = 1, 2, 3, \dots, N \quad (8)$$

Definitions and conversions are:

$$J_m \equiv \rho Y_m v_{m,\eta} = \frac{\rho^2 W_m}{\bar{W}_{mix}^2} \sum_{j \neq m}^N W_j D_{mj} X_j' ; \quad v_{m,\eta} = \frac{\rho W_m}{\bar{W}_{mix}^2 Y_m} \sum_{j \neq m}^N W_j D_{mj} X_j' ; \quad m = 1, 2, 3, \dots, N \quad (9)$$

$$X_m = \frac{\bar{W}_{mix}}{W_m} Y_m ; \quad \bar{W}_{mix} \equiv \sum_{n=1}^N X_n W_n ; \quad m = 1, 2, 3, \dots, N \quad (10)$$

Boundary conditions:

$$f_1'(\infty) = 1 ; \quad f_1'(-\infty) = \sqrt{\frac{1}{\rho_{-\infty}} + \left(\frac{\omega_k}{2S_1} \right)^2 \left(1 - \frac{1}{\rho_{-\infty}} \right)} ; \quad f_1(0) = 0 \quad (11)$$

$$f_2'(\infty) = 1 ; \quad f_2'(-\infty) = \frac{1}{\sqrt{\rho_{-\infty}}} ; \quad f_2(0) = 0 \quad (12)$$

$$Y_m(\infty) = Y_{m,\infty} ; \quad Y_m(-\infty) = Y_{m,-\infty} \quad (13)$$

$$T(\infty) = 1 ; \quad T(-\infty) = T_{-\infty} \quad (14)$$

Inclusion of multi-step chemical kinetics and the associated thermo-physical properties and diffusion formulation was achieved via integration with Cantera [18], an open source toolbox for chemical kinetics, thermodynamics, and transport processes. Cantera allows users to load CHEMKIN-style chemical kinetic models and will compute a host of thermodynamic properties, reaction rates, and transport coefficients. In the present work, we are interested in hydrogen-oxygen-nitrogen flamelets and will use the hydrogen combustion subset of the Foundational Fuel Chemistry Model 1.0 (FFCM-1) developed at Stanford University [19]. This model considers 25 reactions among the following nine species: H₂, O₂, H, O, OH, H₂O, HO₂, H₂O₂, and N₂.

The computational scheme used to obtain the steady-state solutions of the flamelet equations is a hybrid pseudo-time stepping/Newton method, similar to those used in CHEMKIN OPPDIF and Cantera difflame solvers. An initial solution is guessed and iterated in pseudo-time until the faster

Newton method becomes stable and can iterate the solution to convergence. As this paper is primarily concerned with the effects of vorticity near the flammability limit, a steady-state solution is first obtained at a low strain rate to be used as the initial guess at a higher strain rate. The strain rate is sequentially increased in this manner, using the former steady-state solution as the initial guess for a higher strain rate, until the flame extinguishes. This completes computation of the stable (upper) branch of the S-curve. The program then creates a new guess with a lower strain rate and a lower peak temperature and sequentially decreases these parameters to obtain the unstable (middle) branch of the S-curve. Newton’s method is outlined in the following set of equations.

Our system of governing equations has $N + 3$ dependent variables where N is the number of species, i.e., $T, f'_1, f'_2, Y_1, Y_2, Y_3, \dots, Y_N$ for temperature, derivative of the ξ -momentum similarity variable, derivative of the z -momentum similarity variable, and the mass fractions of all species. The computational domain of the counterflow is broken into a variable mesh of n spatial nodes. Let x_l be a $1 \times (N+3)n$ vector containing the spatially-ordered dependent variables existing at all spatial nodes, i.e. $x_l = [T_1, f'_{1,1}, f'_{2,1}, Y_{1,1}, \dots, Y_{N,1}, T_2, f'_{1,2}, f'_{2,2}, Y_{1,2}, \dots, Y_{N,2}, \dots, T_n, f'_{1,n}, f'_{2,n}, Y_{1,n}, \dots, Y_{N,n}]$. Let x_{l+1} be the same vector of dependent variables at the subsequent iteration step, i.e. x_{l+1} is closer to the converged solution set than x_l . Let F be the set of governing equations (Equations 5-8) and F' be the derivative of the governing equations with respect to a change in the dependent variables as shown in Equation 15.

$$F'(x_l) = \frac{F(x_{l+1}) - F(x_l)}{x_{l+1} - x_l} \quad (15)$$

We seek a steady-state solution, which in the framework of Equation 15, means $F(x_{l+1})$ must eventually equal zero. It may then be assumed that x_{l+1} is the converged solution and Equation 15 reduces to Equation 16.

$$F'(x_l)x_{l+1} = F'(x_l)x_l - F(x_l) \quad (16)$$

Recognize Equation 16 is now in the canonical form of a matrix equation, $Ax = B$, and may be solved by inverting the matrix or by various solvers for linear systems of equations. Furthermore, the ODEs given in Equations 5-8 are recast by finite differencing as linear algebraic statements. The program written for this flamelet model uses a built-in linear systems solver in MATLAB called gmres for “generalized minimum residual”. In Equation 16, $F'(x_l)$ is a block-tri-diagonal Jacobian matrix with dimension $(N + 3)n \times (N + 3)n$ and is calculated by computing the derivative of each governing equation with respect to a small perturbation of each dependent variable at every spatial location.

3 Validation

Validation of the rotational flamelet model was performed by comparing its computation results with those obtained from the Cantera diffusion flame code. Here, we present the case of a nitrogen-diluted hydrogen-oxygen counterflow diffusion flame. The oxidizer stream is pure O_2 at 300 K, while the fuel stream is an equimolar mixture of H_2 and N_2 at 300 K. The pressure is set at 10 atmospheres (atm). A maximum strain rate $S_{max}^* = 1,000,000$ (1/s) is maintained. Note that the maximum strain rate is defined locally inside the flame zone. Equal strain rates along the ξ and z directions are considered in the rotational flamelet model. Results in terms of axial velocity, temperature, and mass fraction profiles are compared and shown in Figure 2. There is excellent

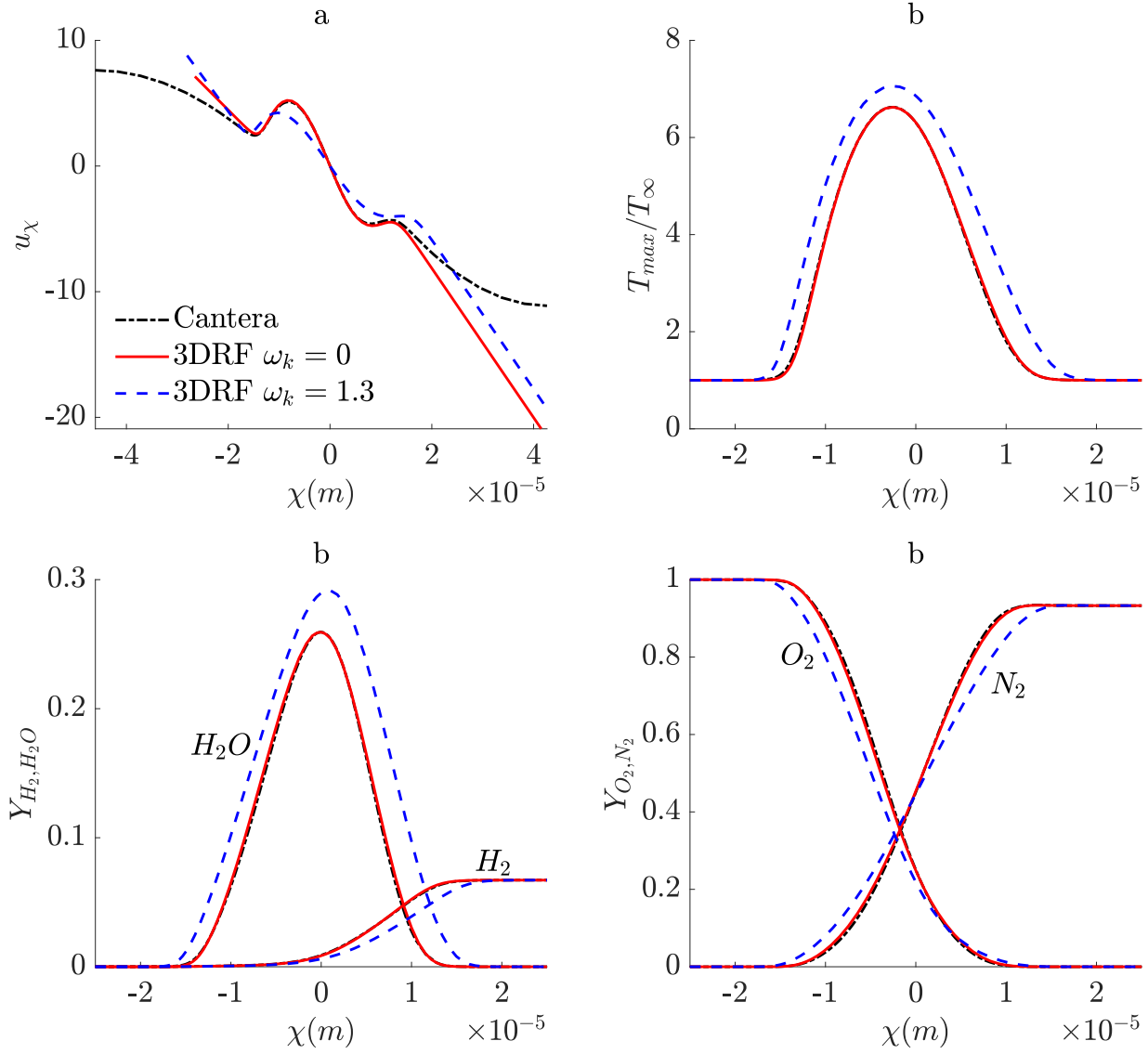


Figure 2: Comparison between rotational flamelet model and Cantera default diffusion flame solver. (a) Axial velocity; (b) Temperature; (c) H_2O and H_2 mass fractions; (d) O_2 and N_2 mass fractions. The maximum strain rate for matched curves is $S_{max}^* = 1,000,000$ 1/s.

agreement in the various profiles within the diffusion layer. Outside the diffusion layer, there are notable differences in velocity as a result of the mathematical framework the two codes are based on. Cantera is based on a nozzle counterflow. This means the fuel and oxidizer streams issue from nozzles at a fixed and finite separation distance. Nozzle flow forces the axial velocity gradient to zero at the boundaries as is seen on the black dash-dot curve in Figure 2 a. The incoming streams for the rotational flamelet in the non-Newtonian frame are instead based on a far-field potential counterflow in which the domain extends from $-\infty$ to ∞ and the axial strain rate is non-zero at the computational boundary. The axial strain rate is constant in the far field, thereby, better describing sub-grid turbulent-flow conditions. A viscous layer exists in the interfacial region of the flamelet. In the rotational model, the dimensional strain rate, S^* , is defined as the asymptotic axial strain

rate in the positive far field. When it comes to extinction behaviors, comparisons between the rotational flamelet model and Cantera or CHEMKIN results are therefore difficult due to different definitions of global strain rates. Nonetheless, the excellent agreement in the flame zones between the rotational flamelet model and the Cantera results demonstrates the validity of the rotational flamelet model. Also shown in Figure 2 are profiles for $\omega_k = 1.3$. This is to demonstrate the vorticity effect plotted in physical space. A full discussion of vorticity effects is given in Sections 4 and 5.

In the example shown in Figure 2, the strain rate for the flamelet is $S_{max}^* = 1,000,000$ (1/s), the flame-zone dimension is approximately $30 \mu m$, and the viscous-layer thickness is $\delta = \sqrt{\nu/S^*} \approx 3 \mu m$ with kinematic viscosity $\nu = O(10^{-5} m^2/s)$. The viscous layer thickness is based on the local $Re = O(1)$ which makes it the same order as the Kolmogorov scale if the flamelet were embedded in a turbulent field. A situation with these conditions would occur on the smallest scale of the turbulent flow if the integral scale had a shear flow with a velocity variation of $O(100 m/s)$ across a shear layer with transverse dimension $O(10 cm)$, which produces $Re = 10^6$ and a strain rate of $O(1000 1/s)$ on the integral scale. The strain rate, velocity, and length sizes would scale as $Re^{1/2}$, $Re^{-1/4}$, and $Re^{-3/4}$, respectively, as we move from the integral scale to the Kolmogorov scale. One implication is that eddies that are an order of magnitude larger than the Kolmogorov scale could distort and affect the flamelet with unsteady behavior. This is a proper issue for future study. In the following section on diffusion flames, note that the flame thickness is several times, up to one order of magnitude, larger than the Kolmogorov scale even near the extinction strain rate. Thus, the flame thickness always exceeds the Kolmogorov scale.

4 Results - Diffusion Flames

We further examine the diffusion flame case discussed in the validation section and examine the impacts of vorticity and transverse strain rates. The same mixture composition and conditions are considered, while the axial strain rate is gradually increased to obtain extinction curves. In addition, three combinations of non-dimensional far-field ξ and z strain rates are used, ($S_1 = 0.75$, $S_2 = 0.25$), ($S_1 = 0.50$, $S_2 = 0.50$), and ($S_1 = 0.33$, $S_2 = 0.67$), and three values of non-dimensional vorticity are applied ($\omega_k = 0.0, 1.0, 1.3$). Note that a single legend applies to all sub-figures.

Figure 3 shows the extinction curves, also referred to as S-shaped curves or simply S-curves, of the diluted hydrogen-oxygen counterflow diffusion flame at various combinations of S_1 , S_2 , and ω_k . These curves clearly demonstrate that imposing vorticity on the counterflow domain extends the flammability limit. When $S_1 = 0.75$, $S_2 = 0.25$, there is a 17.0% increase in the extinction strain rate between vorticity values of $\omega_k = 0$ and $\omega_k = 1.3$. When $S_1 = 0.5$, $S_2 = 0.5$, there is a 30.0% increase in the extinction strain rate for the same range of vorticity. When $S_1 = 0.33$, $S_2 = 0.67$, there is a 16.8% increase in extinction strain rate between $\omega_k = 0$ and $\omega_k = 1$. Differences in S-curve behavior based on magnitudes of S_1 and S_2 are a result of flame stability dependence on mass efflux rates in the ξ and z directions. S_1 and S_2 are indicative of the percentages of outflow leaving the domain along the ξ and z axes, respectively. However, they only give exactly the outflow percentage if $\omega_k = 0$. Note that ξ lies in the plane in which centrifugal force acts on the flow while z is normal to this plane and does not align with a centrifugal force. Thus, when $S_1 > S_2$, a higher percentage of flow exits along the ξ -axis and is accelerated by the centrifugal force, reducing residence time

and leading to earlier extinction (in terms of S^*). Conversely, when $S_1 < S_2$, a higher percentage of flow exits along the z -axis and is not accelerated by centrifugal force. In this case, the residence time is not reduced and may increase depending on the relative magnitudes of S_1 and S_2 . Figure 3 **b** also includes two points at 20 atm. These points indicate the vorticity effect is consistent at elevated pressure.

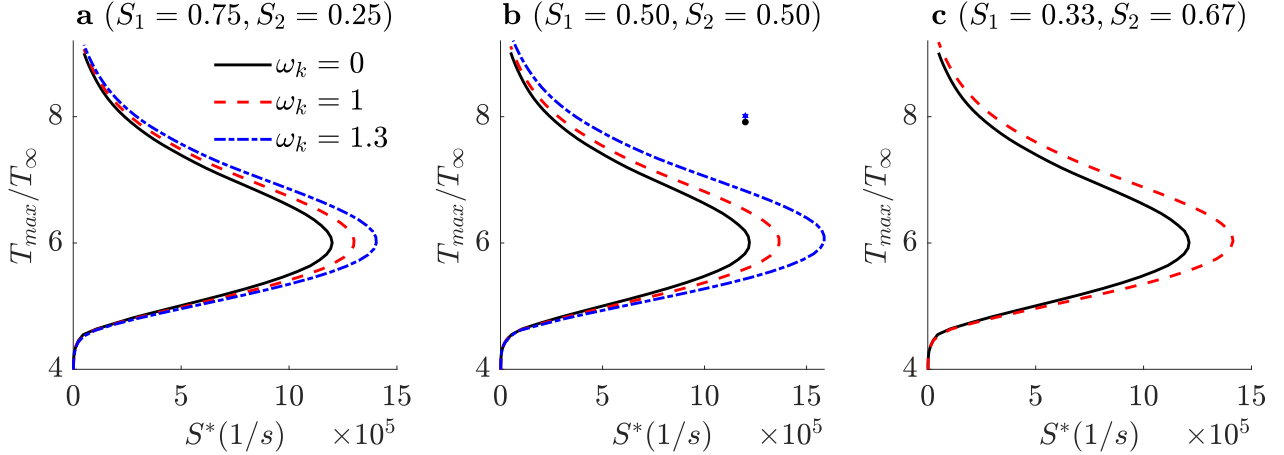


Figure 3: Extinction curves (S-curves) of counterflow diffusion flames with varying strain rate and vorticity magnitudes. The black dot ($\omega_k = 0$) and blue star ($\omega_k = 1.3$) in Sub-figure **b** indicate points on the extinction curves where $S^* = 1,200,000$ 1/s for a background pressure of 20 atm. This is to show the effect of increasing pressure. Note, a point for $\omega_k = 1$ is not shown but falls between the black dot and blue star as expected.

Figure 4 shows three velocity components as well as the similarity variable f , indicative of the axial mass flux, for the symmetric far-field strain rate case $S_1 = 0.5$, $S_2 = 0.5$, and $S^* = 1,200,000$ 1/s. However, the flow is only axisymmetric if $\omega_k = 0$. All values are non-dimensional. Velocity profiles in the ξ and z directions, i.e. u_ξ and w , are divided by their respective spatial variables. Inspection of the slopes of the u_χ velocity profiles (Sub-figure **a**) in the diffusion layer ($-5 \leq \eta \leq 5$) reveals the cause of the increased extinction limits noted in Figure 3. Although the imposed far-field strain rates are the same for all values of vorticity, the strain rate (slope) in the flame zone is reduced as vorticity increases. This essentially allows a flame with vorticity that is highly strained in the far field to behave like a flame without vorticity that is moderately strained in the far field. These effects are most prevalent when the location of minimum density coincides with the location of peak temperature. Additional cases not shown here were performed with pure hydrogen in-flowing from the right instead of the equal-molar hydrogen-nitrogen mixture of the current discussion. In this case, the location of minimum density lies upstream of the stagnation point, toward the fuel inlet boundary, and well outside the flame zone. Under this condition, the outflow is less severely altered by vorticity due to its higher density, and flammability limits are minimally extended. Cases were also tested using water to dilute the hydrogen stream in place of nitrogen. These cases showed no qualitative difference from the nitrogen case.

Examination of the four sub-figures together shows that excess oxygen enters the domain along the η -direction when vorticity is applied. This excess oxygen exits the domain along the ξ -axis as shown by the u_ξ/ξ magnitude between $-20 < \eta < 5$. The introduction of vorticity also causes undulating behavior of the u_ξ and w -velocity components in the flame zone. Without vorticity,

$$S_1 = 0.50, S_2 = 0.50$$

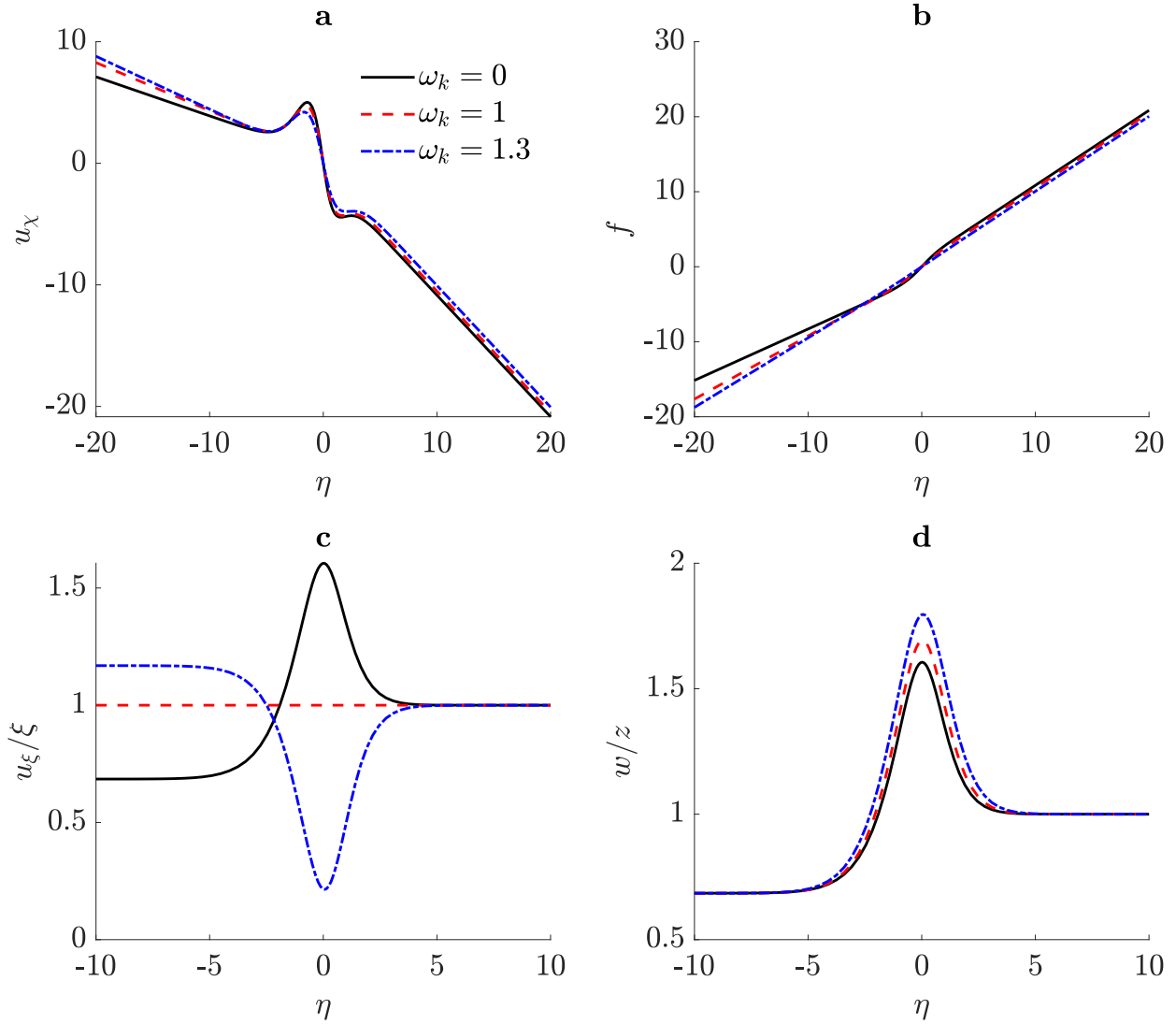


Figure 4: (a) Axial (inflow) velocity u_x ; (b) Similarity variable f ; (c) Transverse outflow velocity normal to vorticity vector divided by length (u_ξ/ξ); (d) Transverse outflow velocity parallel to vorticity vector divided by length (w/z). $S_1 = 0.5, S_2 = 0.5, S^* = 1,200,000$ 1/s.

u_ξ/ξ and w/z are equal, indicating symmetric outflow in the ξ and z directions. Furthermore, we see these velocity components are elevated in the flame zone showing the hot (low-density) products of combustion accelerating out of the domain. However, with strong vorticity, the low-density products of combustion are forced toward the stagnation point in the ξ direction under the centrifugal action of vorticity. This leaves only the z -direction as a path for combustion products to escape which is why the peaks of the w/z curves increase with increasing vorticity. These effects are compounded when the flamelet exists in an asymmetric strain field which is discussed later on.

We now consider the effects of vorticity and transverse strain rates on temperature, species, and energy profiles for the case shown in Figure 4. Figure 5 shows temperature, major species, heat

release rate (HRR), and the integrated H_2 reaction rate profiles for the afore-discussed three cases. Inspection of the temperature profiles shows the direct relationship between peak temperature and vorticity. Next, we examine the species profiles. Unsurprisingly, reactant mass fractions decrease while major product mass fractions increase with vorticity. Essentially, the reduction in strain rate in the flame zone caused by vorticity allows for more complete combustion. Sub-figures **c** and **d** in Figure 5 show the decreased heat release rate and burning rate caused by vorticity. This is the result of decreased mass flux through the domain when the centrifugal force acts on the counterflow as previously noted by [1].

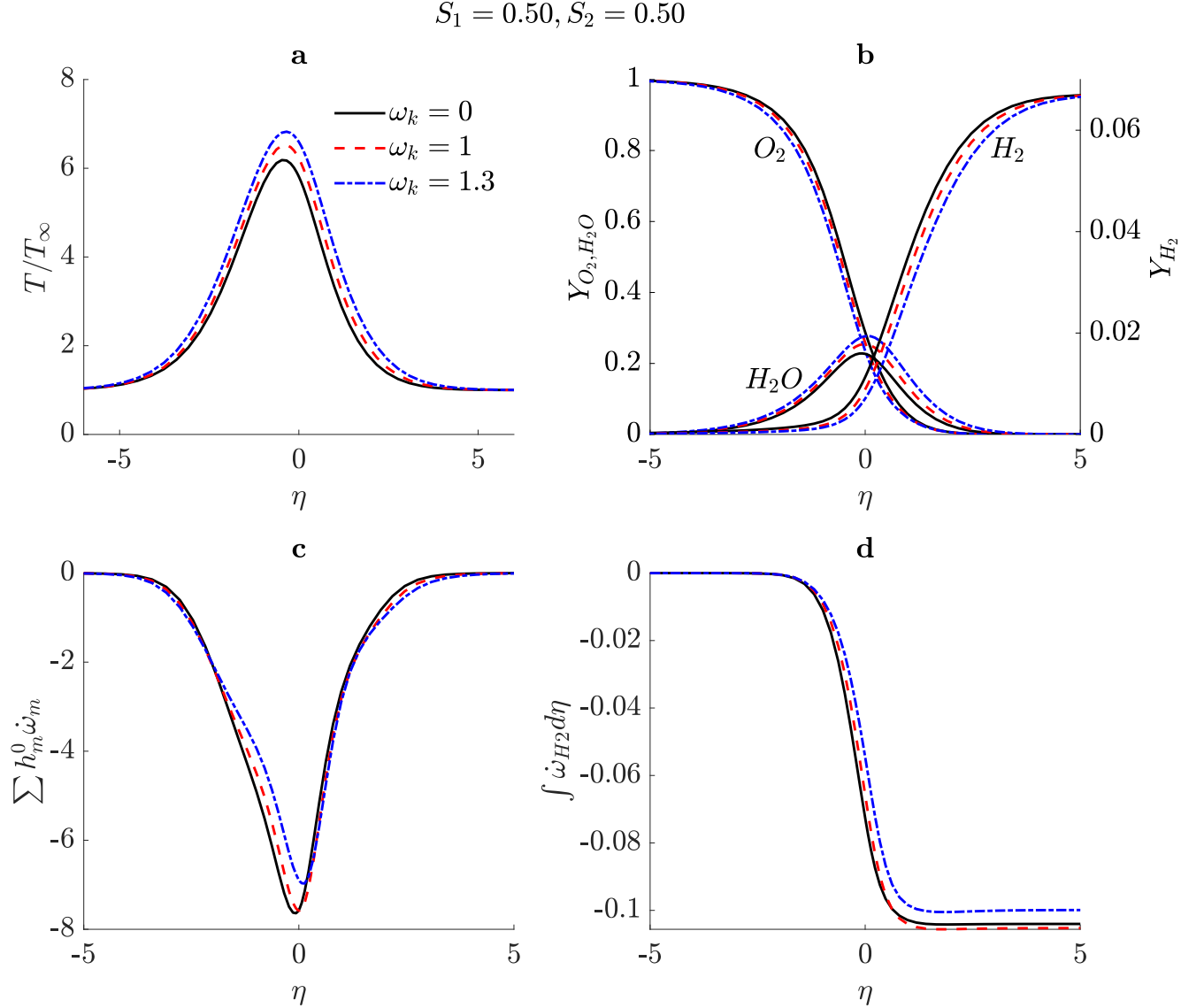


Figure 5: (a) Temperature; (b) Major species mass fractions; (c) Heat release rate; (d) Integrated H_2 reaction rate (burning rate). $S_1 = 0.5, S_2 = 0.5, S^* = 1,200,000$ 1/s.

Besides vorticity, differing strain rates between ξ and z directions can also alter flamelet behaviors compared to equal strain rate scenarios. Figure 6 shows the axial velocity (u_χ) and similarity variable (f) for varying vorticity values ($\omega_k = 0, 1$) and transverse strain rates $S_1 = 0.33, 0.50, 0.75$,

$S_2 = 0.67, 0.5, 0.25$. Note that for the three cases with $\omega_k = 0$ (solid lines), the curves of both the u_χ and f lie within the plotted line thickness of each other and are thus indistinguishable, i.e. all curves for $\omega_k = 0$ are coincident with the solid red line. Certain general trends are unchanged for this asymmetric case, namely the decreased strain rate in the flame zone as well as increased oxygen influx, both a result of imposing vorticity. There is an important difference however. When $S_2 > S_1$, more outflow is allowed in the z -direction which is unrestricted by centrifugal force. This allows more oxygen into the domain and reduces the maximum strain rate in the flame zone. Conversely, when $S_2 < S_1$, the opposite trend is observed.

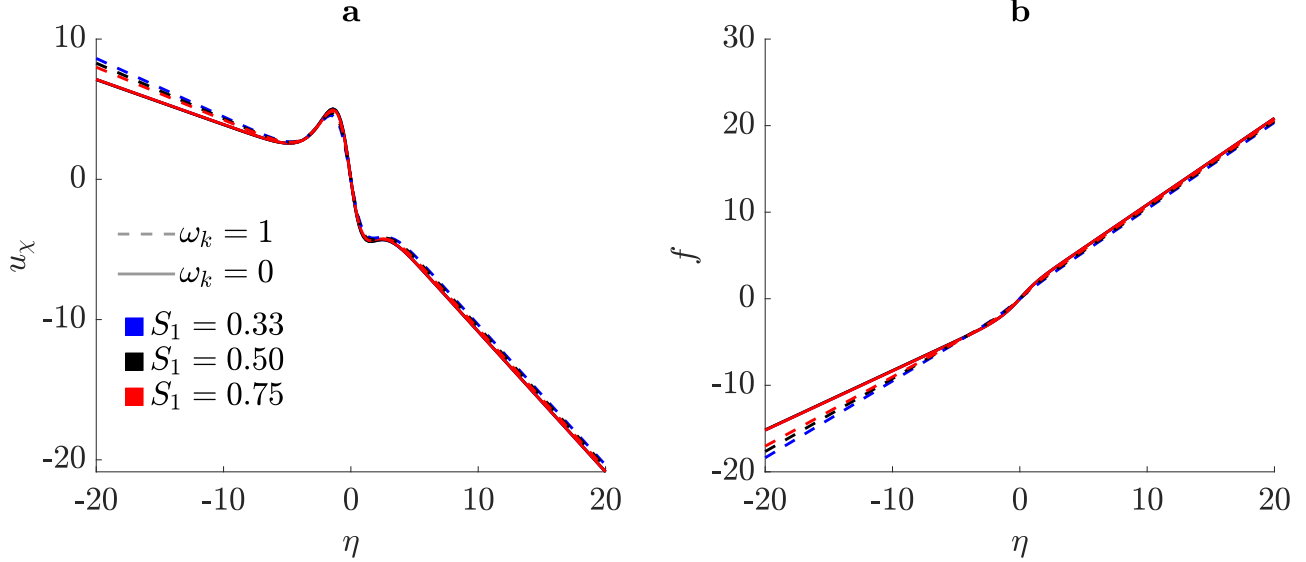


Figure 6: (a) Axial (inflow) velocity u_χ ; (b) Similarity variable f . $S_1 = 0.33, 0.50, 0.75$; $S_2 = 0.67, 0.50, 0.25$, $\omega_k = 0, 1$, $S^* = 1, 200, 000$ 1/s. The three curves on each sub-figure for $\omega_k = 0$ are coincident with the solid red curve.

Figure 7 shows the velocity components in the ξ and z directions for $\omega_k = 0, 1$ and $S_1 = 0.33, 0.50, 0.75$; $S_2 = 0.67, 0.5, 0.25$. First, compare the u_ξ/ξ profiles between Sub-figure **a** and **b** for $S_1 = 0.50$, $S_2 = 0.50$. In Sub-figure **b** a vorticity value of $\omega = 1$ (solid black) produces a straight line due to elimination of any density effect in the ξ -momentum equation (Equation 5) and the boundary condition given by Equation 11. When $\omega \neq 1$ and/or $S_1 \neq 0.5$, the boundary conditions at $-\infty$ and $+\infty$ are not equal, and a straight line does not occur.

Further comparison of the u_ξ/ξ profiles in Figure 7 for the case where $S_1 = 0.75, S_2 = 0.25$ (dash red) shows a conflict of influence in the flame zone between S_1, S_2 , and ω_k . When $S_1 > S_2$, mass efflux is decreased (limited) in the z -direction and increased in the ξ -direction. Because efflux in the ξ - η plane feels the centrifugal effect of vorticity while efflux in the z -direction does not, the centrifugal effect attempts to expel the expanding low-density products of combustion along the z -direction, but the low value of S_2 does not permit this. Instead, due to the bias toward ξ -efflux from $S_1 > S_2$, u_ξ/ξ is forced to remain positive in the flame zone. Comparing this case ($S_1 > S_2$) to the case where ($S_1 < S_2$) (dash-dot blue), we see an alignment between the preferred efflux direction and vorticity magnitude. When vorticity is applied, efflux prefers to flow in z , and is restricted in ξ , which is why u_ξ/ξ becomes negative and the maximum of w/z is much higher for $S_1 < S_2$ than for $S_1 > S_2$. Overall, this results in a lower strain rate in the flame zone and thus

increased residence time which explains why extinction points in Figure 3 **c** occur at a higher strain rate than the corresponding points in Figure 3 **a** and **b**.

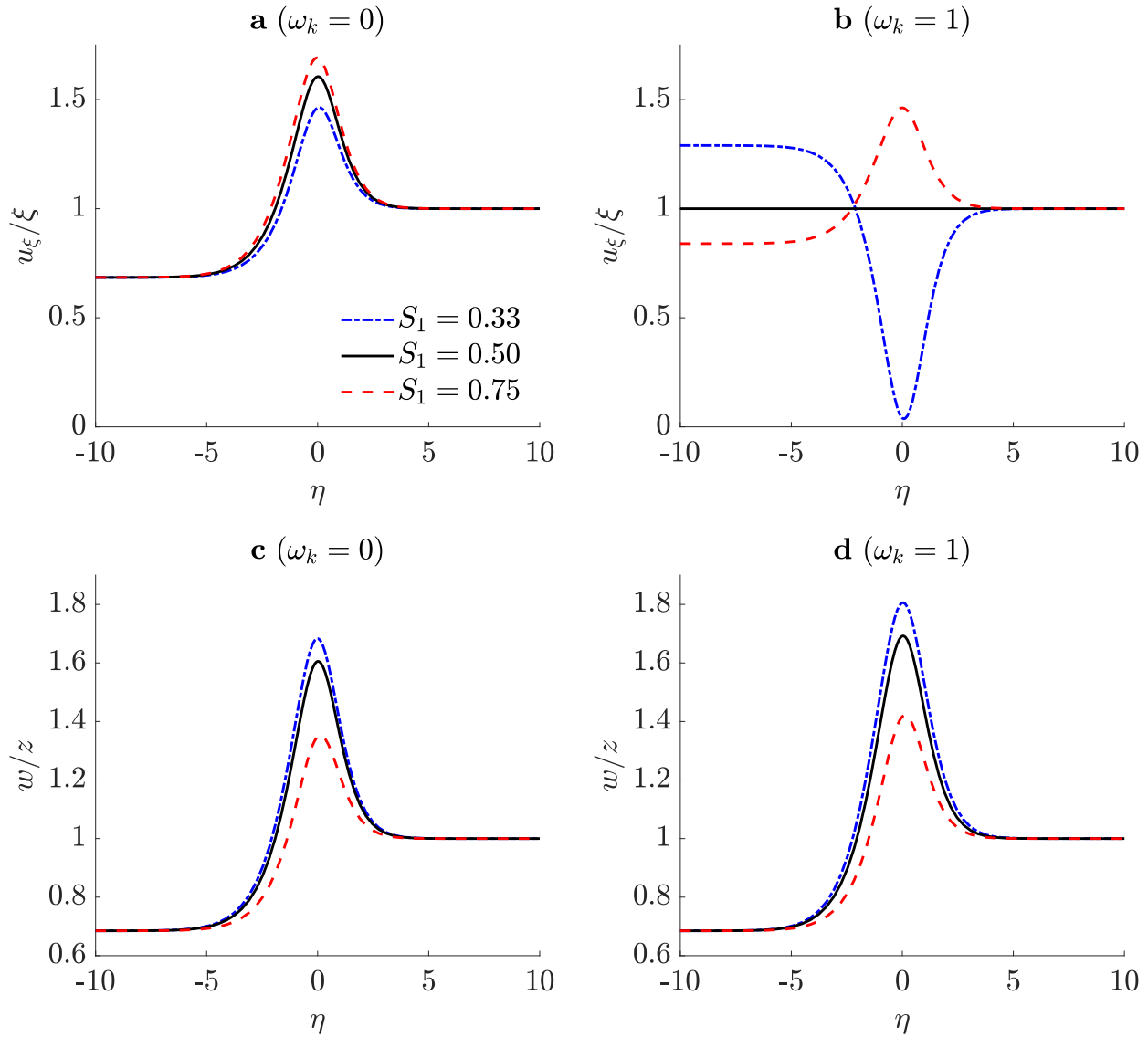


Figure 7: (a) u_ξ/ξ , $\omega_k = 0$; (b) (u_ξ/ξ) , $\omega_k = 1$; (c) (w/z) , $\omega_k = 0$; (d) (w/z) , $\omega_k = 1$. $S_1 = 0.33, 0.50, 0.75$; $S_2 = 0.67, 0.50, 0.25$. $S^* = 1, 200, 000$ 1/s.

Figure 8 shows temperature, major species, heat release rate (HRR), and the integrated H_2 reaction rate for the symmetric and asymmetric strain rate cases at $\omega_k = 0, 1$. Many curves are very close to one another because the scalar quantities are largely a function of axial convection. Axial convection scales with u_χ which shows major differences only in the negative far-field in which there are no scalar gradients. Still, the deviations of strain rate and residence time arising from differing choices of S_1 , S_2 , and ω_k , are reflected in the scalar profiles. When $S_1 < S_2$ and $\omega_k = 1$, we see the minimum strain rate in the flame zone and the largest increase in residence time. Correspondingly, this case produces the highest temperature and highest product mass fraction. Interestingly, this case also produces the lowest HRR magnitude relative to the other rotational cases. When $S_1 > S_2$ and

$\omega_k = 0$, we see the maximum strain rate in the flame zone and a reduction in residence time. This case produces the lowest temperature, lowest product mass fraction, and lowest HRR magnitude of the irrotational cases. Profiles of dependent variables on the unstable branch are qualitatively similar to those on the stable branch.

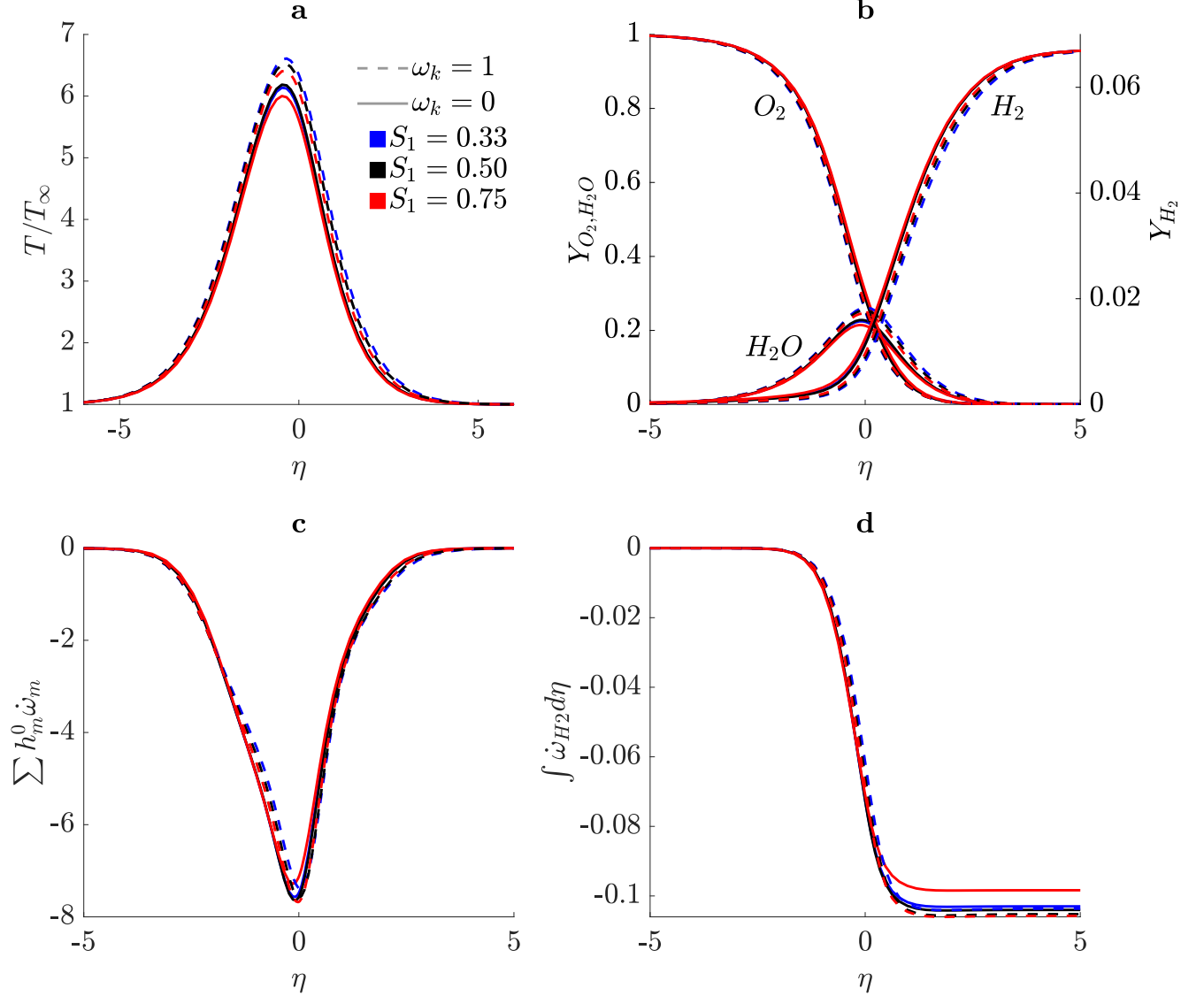


Figure 8: (a) Temperature; (b) Major species mass fractions; (c) Heat release rate; (d) Integrated H_2 reaction rate (burning rate). $S_1 = 0.33, 0.50, 0.75$; $S_2 = 0.67, 0.50, 0.25$. $\omega_k = 0, 1$, $S^* = 1, 200, 000$ 1/s.

There were also found to be limits on the maximum magnitudes of ω_k and S_2 that may be applied to the model. When either of these parameters exceeded a critical value, the momentum generated by centrifugal force overpowers the in-flowing momentum and a reversal of flow occurs near the stagnation point. When this happens a pure counteflow no longer exists, instead resembling the superposition of a counterflow and a source flow.

5 Results - Premixed Flames

Here, we present the case of a stoichiometric hydrogen-air premixed flame. Water at 1800 K enters the domain from at $\eta = -\infty$. A combustible mixture of stoichiometric hydrogen and air at 300 K enters the domain at $\eta = \infty$. The pressure is set at 10 atm. In the following figures and discussion, three combinations of non-dimensional far-field ξ and z strain rates are used, $S_1 = 0.75$, $S_2 = 0.25$, $S_1 = 0.50$, $S_2 = 0.50$, and $S_1 = 0.33$, $S_2 = 0.67$, and two values of non-dimensional vorticity are applied, $\omega_k = 0$ and $\omega_k = 1$.

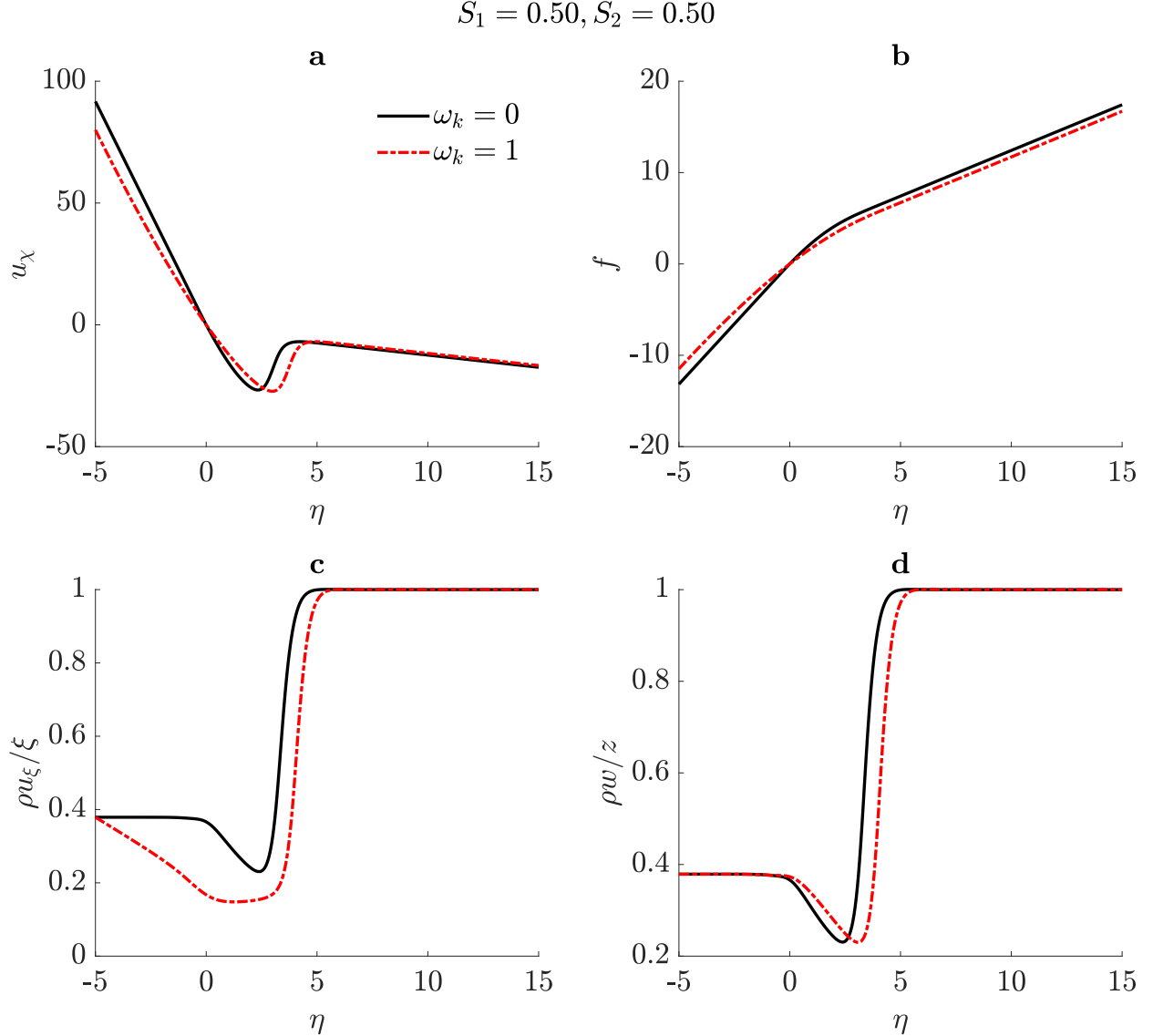


Figure 9: Premixed flame. (a) Axial (inflow) velocity u_χ ; (b) Similarity variable f ; (c) Transverse mass efflux normal to vorticity vector divided by length ($\rho u_\xi/\xi$); (d) Transverse mass efflux parallel to vorticity vector divided by length ($\rho w/z$). $S_1 = 0.5$; $S_2 = 0.5$; $\omega_k = 0, 1$; $S^* = 50,000$ 1/s.

Figure 9 shows axial velocity u_χ , the similarity variable f , and mass effluxes in the ξ and z directions, $\rho u_\xi/\xi$ and $\rho w/z$, respectively, for the symmetric far-field strain rate case $S_1 = 0.5$, $S_2 = 0.5$ at $\omega_k = 0, 1$. These profiles are taken at an intermediate strain rate value of $S^* = 50,000$ 1/s. All values are non-dimensional. Efflux profiles, in the ξ and z directions, are divided by their respective spatial variables. Sub-figures **a** and **b** show a reduction in boundary velocity and mass flux due to the centrifugal effect. Sub-figure **c** shows efflux component $\rho u_\xi/\xi$, is no-longer locally constant near the inflow boundary, and instead immediately decreases to its minimum value when vorticity is applied. This is to satisfy mass conservation as less H_2O is brought into the domain when $\omega_k = 1$. Sub-figure **d** shows only a modest right-ward shift in the efflux $\rho w/z$ when vorticity is applied. This is a result of the increased flame standoff distance.

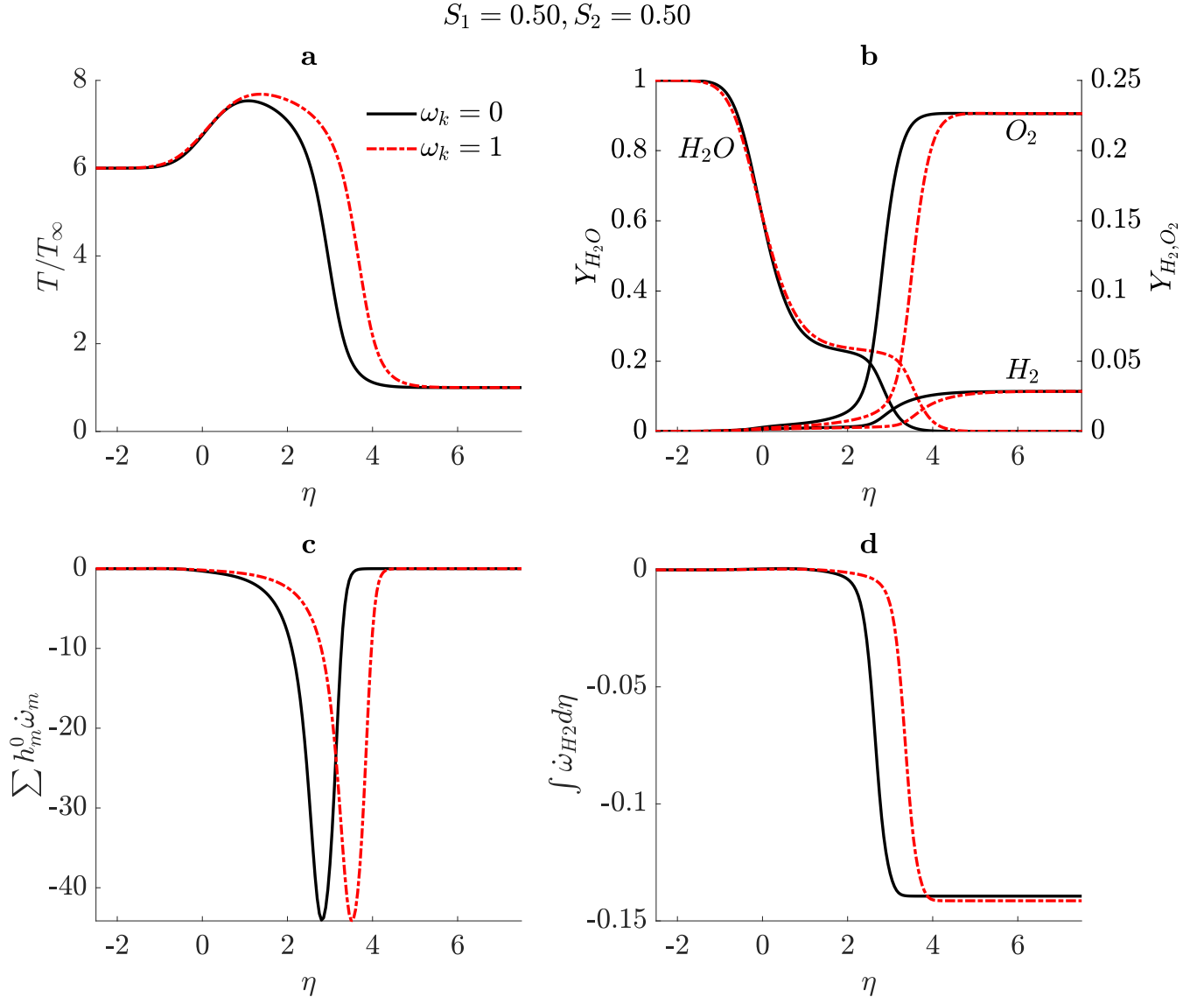


Figure 10: Premixed flame. (a) Temperature; (b) Major species mass fractions; (c) Heat release rate; (d) Integrated H_2 reaction rate (burning rate). $S_1 = 0.5$; $S_2 = 0.5$; $\omega_k = 0, 1$; $S^* = 50,000$ 1/s.

As the premixed flame does not always have a unique peak temperature, the same manner of extinction curves as shown in Figure 3 hold less meaning because the peak temperature does not decay until the flame zone reaches the H_2O diffusion layer. Instead, it is beneficial to discuss location of the flame zone diffusion layer, relative to the H_2O diffusion layer, which does decrease predictably with S^* . Figure 10 **a** shows both an increased peak temperature and increased flame thickness due to the centrifugal effect. Again, vorticity lowers the strain rate in the flame zone, increasing residence time. The species profiles in Sub-figure **b**, heat release rate in Sub-figure **c**, and integrated H_2 reaction rate in Sub-figure **d**, reflect this shift of the diffusion layer. We expect that the incoming temperature of the H_2O stream will affect the flame character near the extinction limit.

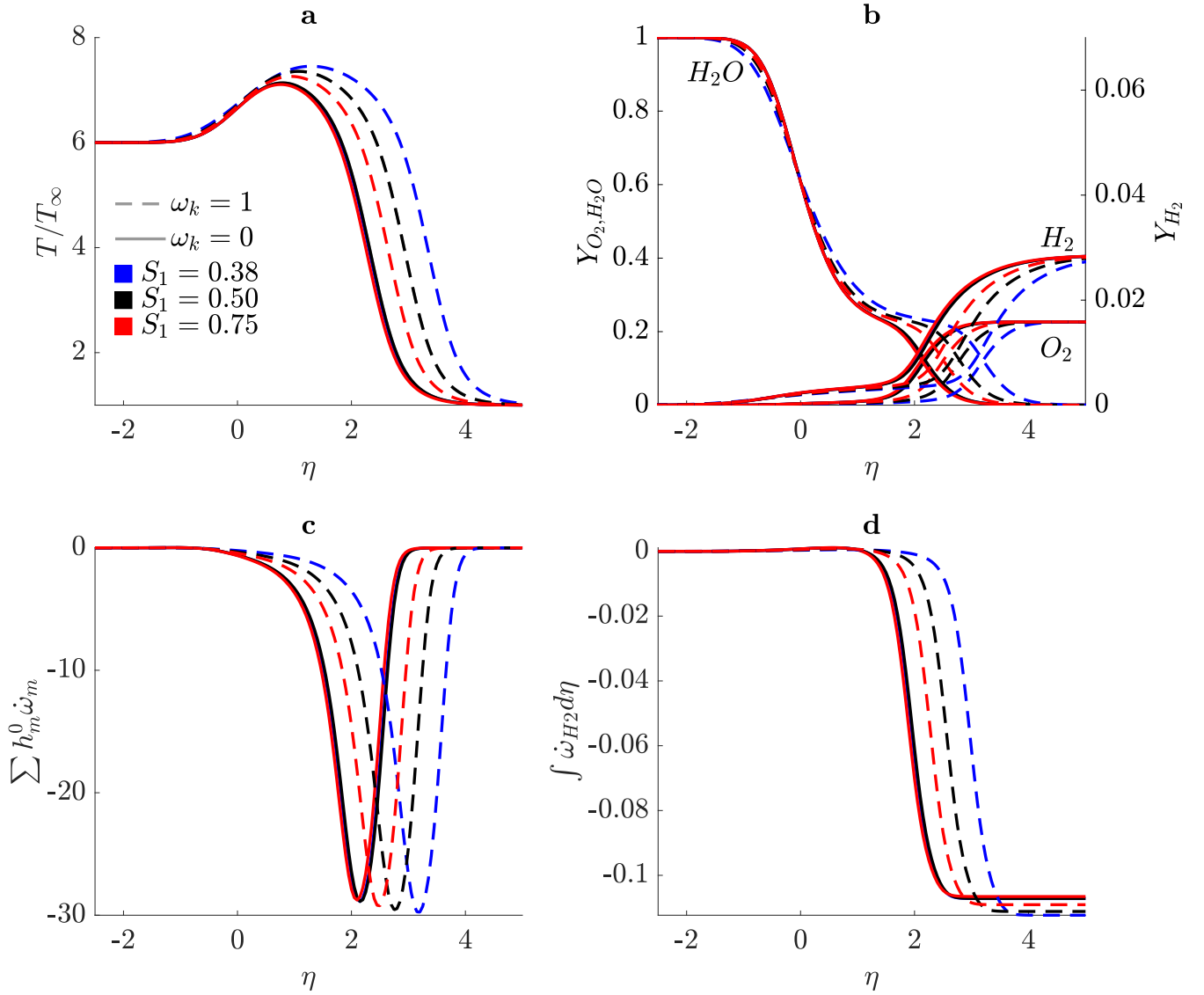


Figure 11: Premixed flame. (a) Temperature; (b) Major species mass fractions; (c) Heat release rate; (d) Integrated H_2 reaction rate (burning rate). $S_1 = 0.38, 0.50, 0.75$; $S_2 = 0.62, 0.50, 0.25$; $\omega_k = 0, 1$; $S^* = 75,000$ 1/s.

Figures 11 and 12 explore the same premixed flame at a higher strain rate of $S^* = 75,000$ 1/s with varying S_1 , S_2 , and ω_k combinations. Note, within these figures, some of the $\omega_k = 0$ curves are coincident and difficult to distinguish. Figure 11 shows that premixed flames are similarly affected by vorticity and $S_2 > S_1$ combination as compared to diffusion flames. Increasing vorticity increases peak temperature and flame standoff distance. We also notice that when $\omega_k = 0$, the case of $S_1 = 0.5, S_2 = 0.5$ produces the highest temperature, as was the case with diffusion flames. Figure 12 shows the velocity and mass flux profiles. These profiles are qualitatively similar to the diffusion flame cases and show similar trends.

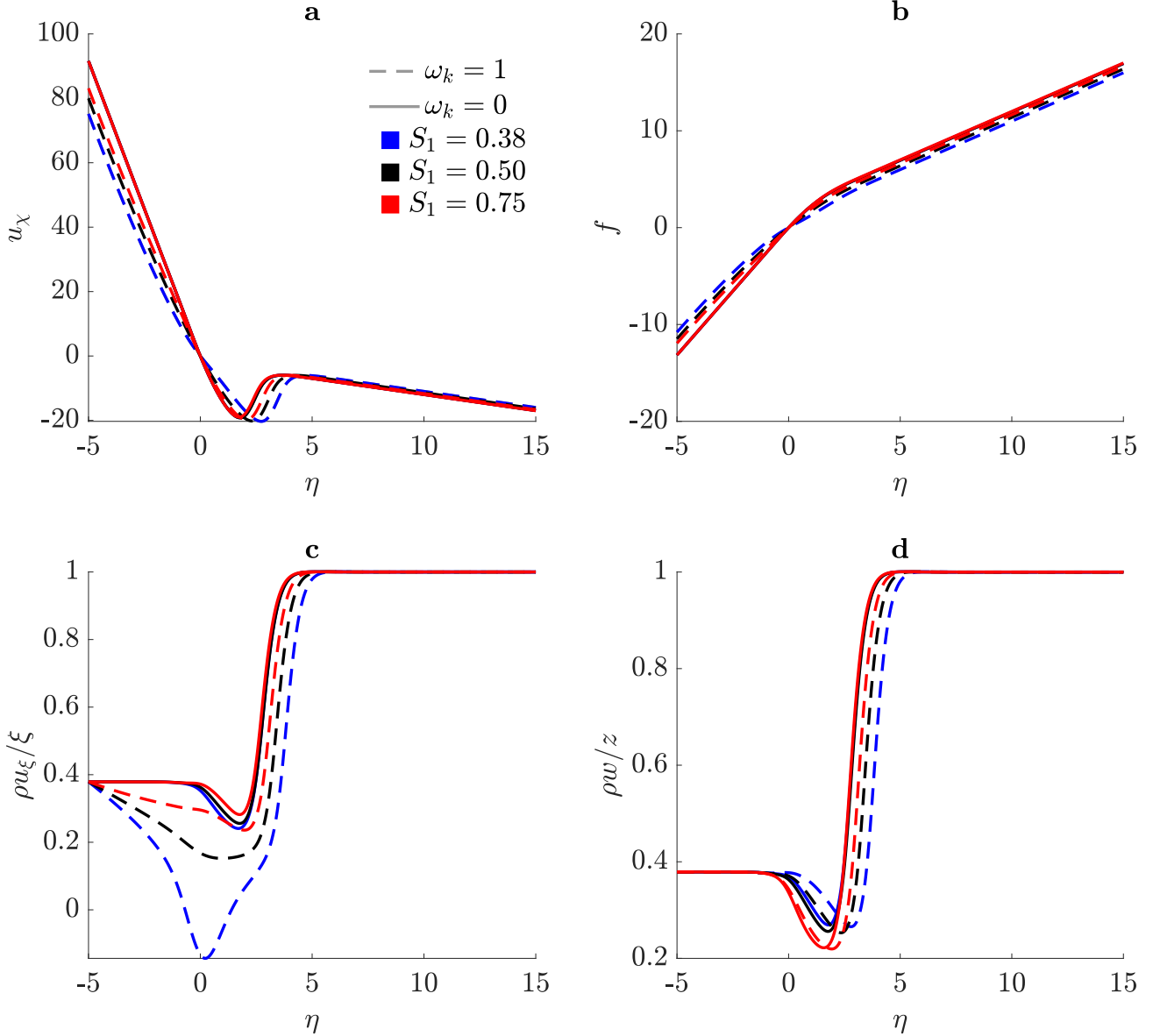


Figure 12: Premixed flame. (a) Axial (inflow) velocity u_χ ; (b) Similarity variable f ; (c) Transverse mass efflux normal to vorticity vector divided by length ($\rho u_\xi / \xi$); (d) Transverse mass efflux parallel to vorticity vector divided by length ($\rho w / z$). $S_1 = 0.38, 0.50, 0.75$; $S_2 = 0.62, 0.50, 0.25$; $\omega_k = 0, 1$; $S^* = 75,000$ 1/s.

6 Conclusions

The inclusion of detailed chemical kinetics, mixture-averaged diffusion, and variable thermo-physical properties in the rotational flamelet model has yielded new findings in the effects of vorticity and three-dimensional strain distributions. While corroborating the fundamental result that vorticity increases residence time, making a highly strained flame behave like a moderately-strained, irrotational flame, differences exist due to reactant composition in concert with centrifugal acceleration. The original demonstration of the rotational flamelet model used oxygen and propane as the reactants, which have, by order of magnitude, comparable molecular weights. Consequently, the location of minimum density coincided with that of peak temperature. Initial testing of the modified model using pure hydrogen and oxygen showed the location of minimum density resides upstream in the hydrogen inflow. When vorticity is applied to this case, the tendency of lighter products to exit the domain along the z -axis, as identified by [1], is not apparent because the fluid in the flame zone is relatively dense despite the elevated temperature. The diffusion flame case discussed in Section 4, using an equimolar mixture of nitrogen and hydrogen in the fuel stream, is more similar in terms of density to the original propane-oxygen configuration and does show this tendency. Replacing nitrogen with water accomplishes a similar density shift and is qualitatively equivalent. This is also expected in the burning of hydrocarbon fuels.

Key findings:

- Counterflow geometry specified by constant far field strain rates better approximates resolved scale cell-averaged strain rates while producing velocity and scalar distributions that match nozzle counterflows near the stagnation point.
- Applying vorticity to counterflow flames increases the flammability limit by reducing maximum strain rate and thereby increasing residence time. This also reduces burning rate.
- When the transverse strain rate in the direction aligned with the vorticity vector (S_2) is larger than the transverse strain rate in the plane normal to the vorticity vector (S_1) i.e., ($S_2 > S_1$), flammability limits are extended relative to the opposite inequality of transverse strain rates i.e., ($S_2 < S_1$).
- Vorticity effects are maximized when the location of minimum density coincides with the location of peak temperature i.e., minimum density occurs within the diffusion layer.

The stable and unstable branches of the extinction curves (S-curves) were calculated, clearly showing the extension of the flammability limit and corroborating the initial findings of [1]. Given that vorticity magnitude is largest at the small length scales where flamelet models apply, and that extinction and re-ignition are ubiquitous in turbulent combustion, the precise calculation of extinction behavior is essential. The addition of the vorticity effect to stable- and unstable-branch calculations more accurately captures this unsteady behavior in turbulent reacting flow LES.

The improved kinetics, transport formulation, and variable thermo-physical properties also allow qualitative comparison with existing counterflow diffusion flame codes, such as CHEMKIN OPPDIF and Cantera diff flame codes. The key finding of this comparison is that the steady-state velocity solution is critically dependent on the flow geometry. Specifically, when the in-flowing streams

are assumed to originate from nozzles with a finite separation distance, a different steady-state solution for velocity is obtained from the rotational flamelet code because nozzles force a zero-velocity gradient at the boundaries. Despite the deviation in velocity near the boundaries, the velocity profiles in the flame zone agree very well when the maximum local strain rate is matched. This is the region where scalar gradients exist and thus temperature and mass fraction profiles match well between Cantera and the rotational flamelet model. The use of a potential counterflow to describe the asymptotic incoming streams better represents the physics of turbulent reacting flows because extinction and re-ignition phenomena are dependent on strain rates. In other words, the potential counterflow geometry allows a sub-grid strain rate scaled upward from the resolved-flow strain rate to be imposed as the boundary condition rather than a prescribed mass flux. Adding resolved-flow vorticity compounds the ability of the flamelet model to capture extinction and re-ignition behavior.

Premixed flame cases were also computed to showcase the ubiquity of the rotational flamelet model. Turbulent reacting flows are not limited to diffusion flames only and it is thus the belief of the authors that it is important for the flamelet model to handle both flame types. It is also noteworthy that the extinction strain rates of premixed flames are 1-2 orders of magnitude less than diffusion flames which suggests poor physical emulation of flamelet models that only consider diffusion flamelets. In future work, partially premixed flames appearing in multi-branched flamelet structures will be studied.

Further work is aimed at increasing the computational efficiency of the model, implementation of a JP-5 chemical kinetic model, production of flamelet tables, and inclusion of triple flames.

Acknowledgements

The research was supported by the Air Force Office of Scientific Research through Grant FA9550-22-1-0191 with Dr. Mitat Birkan as program manager and by the Office of Naval Research through Grant N00014-21-1-2467 with Dr. Steven Martens as program manager. The Melucci family is thanked for the support of the first author through the William and Ida Melucci Space Exploration & Technology Fellowship. Discussions with Professor Feng Liu on the numerical methods were valued.

References

- [1] W.A. Sirignano. Three-dimensional, rotational flamelet closure model with two-way coupling. *Journal of Fluid Mechanics*, 945:A21, 2022.
- [2] W.A. Sirignano. Inward swirling flamelet model. *Combustion Theory and Modelling*, 26:1014–1040, 2022.
- [3] W.A. Sirignano. Stretched vortex layer flamelet. *Combustion and Flame*, 244:112276, 2022.
- [4] C.D. Pierce and P. Moin. Progress-variable approach for large-eddy simulation of non-premixed turbulent combustion. *Journal of Fluid Mechanics*, 504:73–97, 2004.
- [5] K.K. Nomura and S.E. Elghobashi. Mixing characteristics of an inhomogeneous scalar in isotropic and homogeneous sheared turbulence. *Physics of Fluids A*, 4:606–625, 1992.
- [6] K.K. Nomura and S.E. Elghobashi. The structure of inhomogeneous turbulence in variable density nonpremixed flames. *Theoretical and Computational Fluid Dynamics*, 5:153–175, 1993.
- [7] O.N. Boratav, S.E. Elghobashi, and R. Zhong. On the alignment of the a-strain and vorticity in turbulent nonpremixed flames. *Physics of Fluids* 8, 8:2251–2253, 1994.
- [8] O.N. Boratav, S.E. Elghobashi, and R. Zhong. On the alignment of strain, vorticity and scalar gradient in turbulent, buoyant, nonpremixed flames. *Physics of Fluids* 10, 10:2260–2267, 1994.
- [9] W.T. Ashurst, A. Kerstein, R. Kerr, and C. Gibson. Alignment of vorticity and scalar gradient with strain rate in simulated navier–stokes turbulence. *Physics of Fluids*, 30:2343–2353, 1987.
- [10] A. Liñán. The asymptotic structure of counterflow diffusion flames for large activation energies. *Acta Astronautica*, 1:1007–1039, 1974.
- [11] N. Peters. *Turbulent Combustion*. Cambridge University Press, Cambridge UK, 2000.
- [12] A. Hamins, H. Thridandam, and K. Seshadri. Structure and extinction of a counterflow partially premixed, diffusion flame. *Chemical Engineering Science*, 40:2027–2038, 1985.
- [13] W.A. Sirignano. Combustion with multiple flames under high strain rates. *Combustion Science and Technology*, 193:1173–1202, 2021.
- [14] C.F. López-Cámara, A.J. Juanós, and W.A. Sirignano. Strain rate and pressure effects on multi-branched counterflow flames. *Combustion and Flame*, 221:256–269, 2020.
- [15] T.M. Nguyen, P.P. Popov, and W.A. Sirignano. Longitudinal combustion instability in a rocket motor with a single coaxial injector. *Journal of Propulsion and Power*, 34:354–373, 2018.
- [16] T.M. Nguyen and W.A. Sirignano. The impacts of three flamelet burning regimes in nonlinear combustion dynamics. *Combustion and Flame*, 195:170–182, 2018.
- [17] T.M. Nguyen and W.A. Sirignano. Spontaneous and triggered longitudinal combustion instability in a single-injector liquid-rocket combustor. *AIAA Journal*, 57:5351–5364, 2019.

- [18] D.G. Goodwin, H.K. Moffat, I. Schoegl, R.L. Speth, and B.W. Weber. Cantera: An object-oriented software toolkit for chemical kinetics, thermodynamics, and transport processes. <https://www.cantera.org>, 2022. Version 2.6.0.
- [19] G.P. Smith, Y. Tao, and H. Wang. Foundational Fuel Chemistry Model Version 1.0 (FFCM-1), 2016.